Energy Conversion and Management 280 (2023) 116791

Contents lists available at ScienceDirect

Energy Conversion and Management

journal homepage: www.elsevier.com/locate/enconman

An open source framework for advanced Multi-physics and multiscale modelling of solid oxide fuel cells

Wanhui Zhao [a], Valerie J. Pinfield [c], Huizhi Wang [e], Jin Xuan [d], Zhiqiang Niu [b,*]

[a] College of Aeronautical Engineering, Civil Aviation University of China, China
[b] Department of Aeronautical and Automotive Engineering, Loughborough University, United Kingdom
[c] Department of Chemical Engineering, Loughborough University, United Kingdom
[d] Department of Chemical and Process Engineering, University of Surrey, United Kingdom
[e] Department of Mechanical Engineering, Imperial College London, United Kingdom

ARTICLE INFO

Keywords:
Solid oxide fuel cells
Multi-scale modelling
Multi-physics modelling
OpenFOAM

ABSTRACT

Solid oxide fuel cells are high-efficiency renewable energy devices and considered one of the most promising net-zero carbon energy technologies. Numerical modelling is a powerful tool for the virtual design and optimisation of the next-generation solid oxide fuel cells but needs to tackle issues for incorporating the multi-scale character of the cell and further improving the accuracy and computational efficiency. While most of solid oxide fuel cell models were developed based on closed source platforms which limit the freedom of customisation in numerical discretization schemes and community participation. Here, an open source multi-physics and multiscale platform for advanced SOFC simulations consisting of both cell- and pore-scale performance models was developed using OpenFOAM. The modelling aspects are elucidated in detail, involving the coupling of various physical equations and the implementation of the pore-scale electrode in the performance model. The entire platform was carefully validated against experimental data and the other numerical models which were implemented in commercial software ANSYS Fluent and based on the lattice Boltzmann method. The cell-scale model is subsequently employed to study the effects of different fuels, i.e., pure hydrogen and different ratios of pre-reformed methane gas under various operating temperatures. It is found that the cell-scale model reasonably predicts the effects of these parameters on the cell performance, aligning well with the Fluent model. This study further identified the size of representative element volume with respect to the current density for the anode via the pore-scale model where the realistic microstructures reconstructed by a Xe plasma focused ion beam–scanning electron microscopy are employed as computational domains. It is found that a volume element size of 124^3 voxels is sufficient to yield the representative current density of the whole. All these numerical investigations show that OpenFOAM is a potential multi-physics and multi-scale computational platform that is capable of accurately predicting both cell-scale and pore-scale performance and spatial information of solid oxide fuel cells. The developed models are also made public in GitHub to inspire community to further develop around it.

1. Introduction

Societies worldwide are making great efforts to transform their energy systems to become net-zero-carbon and sustainable. As one of the promising green energy technologies, fuel cell technologies help in mitigating greenhouse gas emissions from transport and power plants owing to their outstanding merits such as high efficiency and high energy density. Typical examples are solid oxide fuel cells (SOFCs) which have a series of excellent properties such as relative tolerance towards fuel impurities and no requirement for expensive and rare platinum as catalysts. However, to further extend the use of SOFCs, there are more

Abbreviations: ASL, Anode support layers; BV, Butler-Volmer; CFD, Computational fluid dynamics; CSL, Cathode support layers; CO, Carbon monoxide; CH_4, Methane; FCs, Flow channels; FIB-SEM, Focus ion beam-scanning electron microscopy; LBM, Lattice Boltzmann method; LSM, $La_{1-x}Sr_xMnO_3$ (LSM); MSRR, Methane steam reforming reaction; MC, Monte Carlo; Ni, Nickel; OCV, Open circuit voltage; PISO, Pressure implicit with splitting of operators; REV, Representative element volume; SOFCs, Solid oxide fuel cells; SLs, Supporting layers; TPB, Three-phase boundary; WGSR, Water gas shift reaction; YSZ, Yttria-Stabilised Zirconia; 1D, One-dimensional; 2D, Two-dimensional; 3D, Three-dimensional.

* Corresponding author.
E-mail address: Niu@lboro.ac.uk (Z. Niu).

https://doi.org/10.1016/j.enconman.2023.116791
Received 4 November 2022; Received in revised form 3 February 2023; Accepted 4 February 2023
Available online 11 February 2023

Nomenclature

A_v	reactive surface area per unit volume (m^2m^{-3})
d	pore diameter (m)
D	gas diffusivity (m^{-2} s^{-1})
E_{OCV}	open circuit voltage (V)
E_{act}	activation energy (J•mol^{-1})
F	Faraday's constant (C/mol)
j_0	Equilibrium exchange current density (Am^{-2})
J	exchange current density (Am^{-3})
k	adjustable parameter
m	adjustable parameter
M	molecular weight (k mol^{-1})
n_e	number of electrons
p	pressure (Pa)
R	universal gas constant (J/mol K^{-1})
S	source term (kg m^{-3} s^{-1}, or mol/m^{-3} s^{-1})
t	time
T	gas temperature (K)
V	special Fuller diffusion volume (m^{-3} mol^{-1})
Vout	output voltage (V)
Y	mass fraction

Greek letters

α	transfer coefficient
β	transfer coefficient
γ	adjustable parameter
ε	porosity
η	overpotential (V)
μ	dynamic viscosity, kg m^{-1} s^{-1}
ξ	zone indicator
ρ	density, kg m^{-3}
τ	tortuosity
τ_{con}	time constant
φ	potential (V)
ϕ	arbitrary passive scalar
ω	volume fraction of electron conducting particles

Subscripts and superscripts

a	anode
act	activation
c	cathode
eff	effective
ele	electron
tpb	triple-phase boundary
con	constant

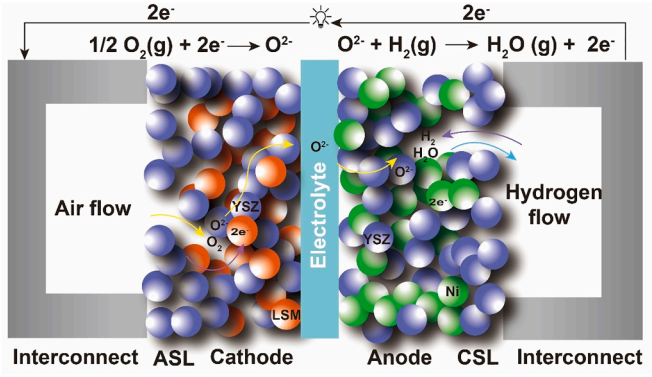

Fig. 1. Schematic of cell structures, physical and electrochemical processes in a typical SOFC.

challenges that need to tackle, including comprehensive optimisation of the cell operating parameters and innovative design of electrode structures.

In general, a typical SOFC consists of a dense electrolyte (e.g. Yttria-Stabilised Zirconia (YSZ)) sandwiched by two porous electrodes (anode and cathode), anode/cathode support layers (ASL and CSL) and interconnect. The present study mainly focuses on the traditional SOFC structure to compare the model with available models and experiments in literature. Ni/YSZ has been a popular choice to fabricate the SOFC anode because of their excellent electrochemical activity for hydrogen oxidation and high stability under SOFC operating conditions. $La_{1-x}Sr_xMnO_3$ (LSM)/YSZ is a classic cathode composite which can enhance electronic conductivity. In an operating SOFC, oxygen ions are produced at the three-phase boundary (TPB) which is the junction of metal, support, and gas phases in the cathode and transports to the anode through the electrolyte where oxygen ions are combined with hydrogen to produce water vapor, as shown in Fig. 1.

Due to the intrinsically multi-physics and multi-scale characters, numerical modelling has been regarded as a cost-effective method to enhance the understanding of the complex interplay among various transport and reaction processes and the effects of porous mesoscale electrode microstructures on the cell performance and long-term durability [1]. A series of numerical models with various fidelity has been reviewed by Wang et al. [2]. A significant proportion of the effort has been made by the community to develop cell-scale models which represent the transport properties of electrodes with a series of empirical or semi-empirical correlations. Kupecki et al. [3] developed a one-dimensional (1D) model to predict the dynamic behaviours of a 60-cell SOFC stack operating with direct internal reforming of the fuel. The 1D SOFC model is capable of quickly predicting the performance of a SOFC stack operating under non-stationary and stationary conditions by accounting for various components of the fuel, electrochemical reactions, as well as mass and heat transport. Shen et al. [4] developed a two-dimension (2D) SOFC model to study the effects of a mixed ionic and electronic conducting electrolyte. The model not only considered the mass transport, electrochemical reactions and charge transport, but also applied a new differential equation of the oxygen pressure to investigate the in-plane electronic current density. Zhu et al. [5] developed a 2D anode-supported SOFC model to study chemically reacting flow in the flow channel and electrode. An important function of the model is to represent elementary heterogeneous chemical kinetics in the form of multistep reaction mechanisms. Sohn et al. [6] integrated simplified 2D macroscale and microscale models to consider mass and heat transfer. Their model reveals the effects of a series of operating parameters including flow configurations, temperature and flow rates of the inlet in an intermediate-temperature SOFC.

Although these 1D and 2D models are reasonably accurate and efficient, they ignored the effects of heterogeneous properties of SOFCs along the in-plane direction. Thus, a series of three-dimensional (3D) SOFC models have been further developed to study various 3D characteristics of SOFCs such as the effects of the flow channel, the local distribution of the temperature, reactant concentration and so on. Lin et al. [7] developed a comprehensive 3D mechanistic model of an anode-supported SOFC to quantitatively evaluate the cell nonuniformity caused by the flow rate, operating voltage and CO electrochemical oxidation. Similar 3D models have been applied by Zhan et al. [8] and Liu et al. [9] to study the effects of metal foam as the novel cathode flow distributor and optimise rib design, respectively. Their results showed that 3D models are imperative when it comes to study spatially sensitive characters of SOFCs. Kakaç et al. [10] reviewed various numerical and

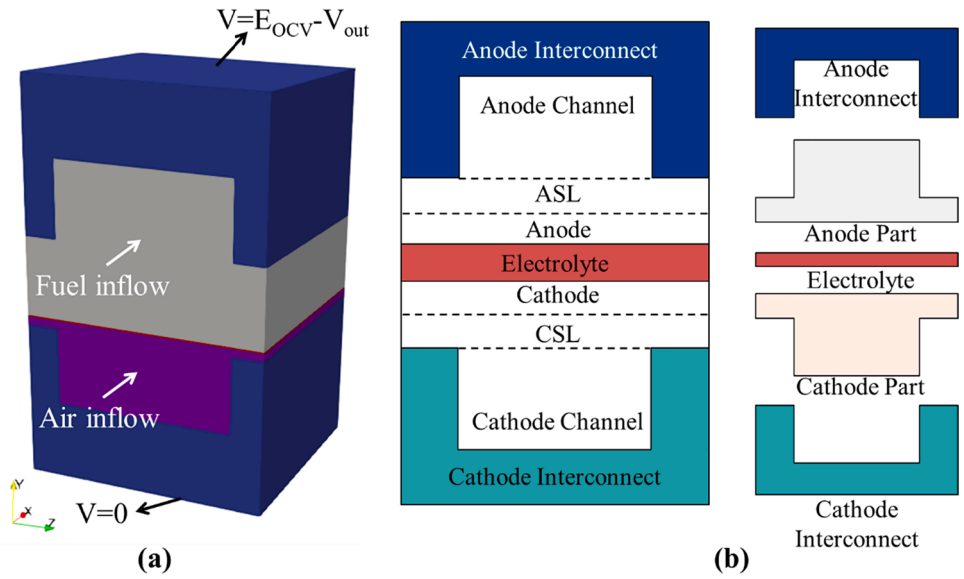

Fig. 2. Schematic diagram of the computational domain in the cell-scale model.

mathematical models for different geometric configurations. More macroscopic modelling of SOFCs for various applications was reviewed by Bao et al. [11].

These stack-level and cell-scale models have greatly advanced the fundamental understanding and substantially contribute the design and optimisation of the high-performance SOFCs. However, a series of electrochemical reactions and transport processes rely upon the microstructures of electrodes, which are largely ignored by the cell-scale models [12]. Comprehensive understanding of the physical and electrochemical processes at pore-scale is critical to rationalise the novel electrode design (e.g. porosity distribution, ratio of different composites) for the next-generation SOFCs. Thus, pore-scale modelling is expected to reveal the dependence of the cell performance on a series of microstructural properties by directly simulating the microstructures of the electrodes. Chen et al. [13] developed a multi-scale model consisting of a generalized percolation micromodel and a multi-physics single-cell model to study the effects of mixed conducting materials. The accuracy of the model was validated against 25 experimental polarization curves in the literature. Mozdzierz et al. [14] employed a FIB-SEM technique to reconstruct 3D electrode microstructures of SOFCs and quantified microstructural parameters used in a cell-scale model. Their study indicates that considering electrode microstructures is a crucial factor in solid oxide fuel cell modelling. Cai et al. [15] developed a 3D pore-scale model to link the microstructure of the electrode to its performance. In their model, the 3D microstructures of the electrode were synthesized via a Monte Carlo (MC) packing method. These microstructures were further coupled with a volume of fluid method to capture interface information and various transport and electrochemical equations to predict the overall cell performance. Motivated by the power of the MC method in synthesizing digital microstructures of SOFCs, Wu et al. [16] further developed a pore-scale model based on the cathode microstructures synthesized by an MC model to optimise the cathode and enhance the electrode connectivity. Paralleled with the fast development of MC-based pore-scale models, phase field models provide more alternatives to synthesize digital microstructures for pore-scale models. In order to study the effects of Ni coarsening on the cell performance, a phase field model and pore-scale multi-physics model were integrated by Wang et al. [17]. In their model, the phase field model synthesized dynamic microstructures of the SOFC anode, which were subsequently input to a multi-physics model to evaluate the electrochemical performance. This model highlighted the effects of Ni content on the microstructure evolution during the cell degradation.

However, assumptions are unavoidable during the synthesis of these digital microstructures based on MC and phase field models, such as the distribution of particle size and initialization of phase distribution. To fully incorporate realistic microstructural information in the pore-scale model, advanced imaging techniques have been employed to reconstruct 3D real digital microstructures of SOFC electrodes for the pore-scale models. Advanced imaging techniques, such as micro-X-ray imaging technology, have been employed to reconstruct anode microstructures which are generally integrated with the lattice Boltzmann method (LBM) to analyse the activation thickness [18] and effects of heterogeneity on a SOFC with direct internal reforming [19]. Limited by the high cost of imaging facilities, very few digital electrode microstructures of SOFCs have been available so far, which leads to the slow progress of pore-scale study with respect to the overall performance of SOFCs. Recently, Hsu et al. [20] adopted a high-resolution Xe plasma focused ion beam–scanning electron microscopy (Xe FIB-SEM) to reconstruct both cathode and anode of a SOFC. The electrode microstructures published by this work provide great opportunities to comprehensively study the relationship between pore-scale behaviours in realistic electrodes and the electrochemical performance of SOFCs.

It is noted that most of the cell-scale and pore-scale models were implemented in commercial platforms such as ANSYS Fluent and COMSOL, which provide limited opportunity to customise the advanced numerical algorithm (e.g., numerical discretization schemes) and specific solvers. Though commercial platforms provide space for the customization of solvers to some extent, the developed specific solvers are always unavailable for the public, therefore blocking community participation. Though several efforts were made to develop open source SOFC solvers [21], the transport and electrochemical reactions in porous electrodes were simplified. Moreover, it is challenging to integrate the physical equations and microstructural domain together in a pore-scale model based on those commercial platforms and a more appropriate and clear methodology is strongly desired. An open source software, OpenFOAM, has emerged in the last decade as a popular numerical platform which provides researchers with huge opportunity to customise solvers and specific algorithms. Thus, this study aims to elucidate the cell-scale and pore-scale modelling aspects of an SOFC and to pave the new modelling route towards intelligent and comprehensive digital study of SOFCs. Both models are validated comprehensively against the results from experiments and relevant numerical models implemented in other numerical platforms such as lattice Boltzmann method (LBM) and commercial computational fluid dynamics (CFD) software ANSYS

Table 1
Geometry and cell mesh of the computational domain for the cell-scale model [22].

Parameters	Value	Number of mesh elements
Channel length, height (mm)	100, 0.5	100, 10
Cell width (mm)	3	30
Rib height, width (mm)	0.5, 0.5	10, 10
Anode diffusion layer thickness (μm)	500	10
Anode catalyst layer thickness (μm)	10	10
Cathode diffusion layer thickness (μm)	40	10
Cathode catalyst layer thickness (μm)	10	10
Electrolyte thickness (μm)	10	10

Table 2
Source terms for governing equations of the cell-scale model.

Source terms	Unit
$S_m = \begin{cases} 0 Channels \\ S_{H_2} + S_{CH_4} + S_{CO} + S_{H_2O} + S_{CO_2} ASL/Cathode \\ S_{O_2} Cathode \end{cases}$	kg m^{-3} s^{-1}
$S_u = \begin{cases} 0 Channels \\ -\frac{\mu}{k_g}\varepsilon^2 \vec{u} SLs, Anode, Cathode \end{cases}$	kg m^{-2} s^{-2}
$S_{CH_4} = -R_{MSRR} M_{CH_4}$ Anode, ASL	kg m^{-3} s^{-1}
$S_{H_2} = \begin{cases} (3R_{MSRR} + R_{WGSR}) M_{H_2}$ ASL $\\ (3R_{MSRR} + R_{WGSR} - \frac{J_a}{2F}) M_{H_2}$ Anode $\end{cases}$	kg m^{-3} s^{-1}
$S_{CO} = \begin{cases} (R_{MSRR} - R_{WGSR}) M_{CO}$ ASL $\\ (R_{MSRR} - R_{WGSR} - \frac{J_a}{2F}) M_{CO}$ Anode $\end{cases}$	kg m^{-3} s^{-1}
$S_{H_2O} = \begin{cases} (-R_{MSRR} - R_{WGSR}) M_{H_2O}$ ASL $\\ (-R_{MSRR} - R_{WGSR} + \frac{J_a}{2F}) M_{H_2O}$ Anode $\end{cases}$	kg m^{-3} s^{-1}
$S_{CO_2} = \begin{cases} R_{WGSR} M_{CO_2}$ ASL $\\ (R_{WGSR} + \frac{J_a}{2F}) M_{CO_2}$ Anode $\end{cases}$	kg m^{-3} s^{-1}
$S_{O_2} = \begin{cases} -\frac{J_c}{4F} M_{O_2}$ Cathode $\\ 0$ Channels, SLs, Anode $\end{cases}$	kg m^{-3} s^{-1}
$S_{ele} = \begin{cases} -J_a$ Anode $\\ J_c$ Cathode $\end{cases}$	Am^{-3}
$S_{ion} = \begin{cases} J_a$ Anode $\\ -J_c$ Cathode $\end{cases}$	Am^{-3}

Fluent. A series of parametric studies will be conducted to demonstrate the model ability in accurately predicting the effects of different operating conditions and fuels, such as pure hydrogen and different ratios of pre-reformed methane gas. In particular, a realistic anode microstructure reconstructed by a Xe FIB-SEM is adopted in the pore-scale model to identify the size of representative element volume element with respect to the overall cell performance. To further reveal the effects of structural parameters of the SOFC electrode, four digital anode microstructures synthesized by a stochastic algorithm will be evaluated by the pore-scale model. In this study, though the hydrogen and pre-reformed methane gas are mainly considered, both models can take multiple fuels such as methane, syngas and methanol etc.

The originality of the study is that it integrates the cell- and pore-scale SOFC modelling into an open-source platform, which opens an opportunity for the community to conduct efficient digital design and optimisation at various scales. The present work is organized as follows: Section 2 describes the governing equations and boundary conditions as well as the numerical settings used in the single cell- and pore-scale models; the models are comprehensively validated against various experimental data and numerical models, presented in Section 3.1. Subsequently, a parametric study is conducted to further study the electrochemical performance of SOFCs with different fuels in Section 3.2. In Section 3.3, the REV size with respect to the current density is determined by the pore-scale model and the effects of different synthetic anode microstructures are studied.

2. Methods

The development of the cell- and pore-scale SOFC models is different in governing equations, computational domains and boundary conditions. The detailed implementation of the two models is presented in Section 2.1 and 2.2 in detail.

2.1. Cell-scale model

The cell-scale model includes all components in a typical SOFC and considers all relevant transports and electrochemical reactions occurring in different components. The cell-scale model assumes microstructural electrodes as homogeneous media according to porous media transport theory. The cell-scale model is developed for a typical anode-supported planar SOFC. The computational cell consists of four kinds of components: anode/cathode flow channels (FCs), ASL and CSL, a Ni/YSZ anode, an LSM/YSZ cathode and a YSZ electrolyte layer, as shown in Fig. 2 (a). Hydrogen and air are supplied in the anode/cathode flow channels, respectively. The geometric parameters of the cell are listed in Table 1. Several assumptions are made in the cell-scale model: i) the cell operates isothermally; ii) the flow of the gas mixtures is laminar and incompressible ideal gas flow; iii) the transport properties of SLs and CLs are isotropic.

2.1.1. Governing equations

Chemical model

Chemical and electrochemical reactions occur simultaneously within the porous electrode when methane (CH_4) and carbon monoxide (CO) are fed into SOFCs. CH_4 and CO can be oxidized by the methane steam reforming reaction (MSRR) and water gas shift reaction (WGSR), respectively, which are expressed as below.

Msrr

$$CH_4 + H_2O \leftrightarrows CO + 3H_2 \quad (1)$$

Wgsr

$$CO + H_2O \leftrightarrows CO_2 + H_2 \quad (2)$$

The reaction rates of the reaction (1) and (2) are consistent with the Ref. [22] and [23]. Due to the lack of catalyst, the reaction in the flow channel is negligible. The reaction rates for MSRR and WGSR are calculated by [24] as below:

$$R_{MSRR} = k_{rf}\left(P_{CH_4}P_{H_2O} - \frac{P_{CO}(P_{H_2})^3}{K_{pr}}\right) \quad (3)$$

$$R_{WGSR} = k_{sf}\left(P_{H_2O}P_{CO} - \frac{P_{H_2}P_{CO_2}}{K_{ps}}\right) \quad (4)$$

where P is the gas partial pressure; k_{rf}, K_{pr}, k_{sf}, and K_{ps} are temperature-dependent parameters [23], which are calculated as following:

$$k_{rf} = 2395\exp\left(\frac{-231266}{RT}\right) \quad (5)$$

$$K_{pr} = 1.0267 \times 10^{10} \times \exp\left(-0.2513Z^4 + 0.3665Z^3 + 0.5810Z^2 - 27.134Z + 3.277\right) \quad (6)$$

$$k_{sf} = 0.0171\exp\left(\frac{-103191}{RT}\right) \quad (7)$$

$$K_{ps} = \exp\left(-0.2935Z^3 + 0.6351Z^2 + 4.1788Z + 0.3169\right) \quad (8)$$

$$Z = \frac{1000}{T(\mathrm{K})} - 1 \quad (9)$$

The Eqn. (4) is fitted by Haberman et al. [24] from high temperature (1073 K – 1163 K) SOFC experiments from Lehnert et al. [25] to

Table 3
Cell-scale model parameters.

Parameters	Symbol	Value
Anode transfer coefficient	α_a	0.5
Cathode transfer coefficient	α_c	0.5
Electronic conductivity (S•m^{-1}) [22]	k_{ele}	$\frac{(9.5\times10^7)}{T(\mathrm{K})}exp(\frac{-1150}{T(\mathrm{K})})$ Anode
		$\frac{(4.2\times10^7)}{T(\mathrm{K})}exp(\frac{-1200}{T(\mathrm{K})})$ Cathode
Ionic conductivity (S•m^{-1}) [22]	k_{ion}	$33.4\times10^3\exp(\frac{-10300}{T(\mathrm{K})})$
Porosity	ε	0.3
Pore diameter (μm)	d	1.0
Operating pressure (atm)	P	1.0
Tortuosity	τ	6.0 [16]
Faraday's constant (C/mol)	F	96487.0
Adjustable fitting parameter 1	γ_{H_2}	1.35×10^9 [16]
Adjustable fitting parameter 2	γ_{CO}	6.14×10^8 [16]
Adjustable fitting parameter 3	γ_{O_2}	9.0×10^7 [16]
Activation energy in anode (J/mol)	$E_{act,a}$	110,000 [19]
Activation energy in cathode (J/mol)	$E_{act,c}$	130,000 [19]
Time constant	τ_{con}	1×10^9
Transfer coefficients	α and β	1,0.5 [22]

describe the WGS reaction rate. The Eqn. (4) has been widely adopted for the calculation of WGSR rate in modelling various SOFCs, e.g., syngas-fueled SOFCs [26] and direct carbon SOFCs with H2O and CO2 as gasification agents [27], and proven to be accurate to predict SOFC performance. Since. The reaction kinetic equation should be updated when the operating pressure significantly differs atmospheric conditions because the reaction kinetics varies when the operating pressure and temperature change [28]. In this study, the Eqn. (4) works under atmospheric pressure.

Mass and momentum conversation

Mass and momentum equations are solved in gas channels and porous electrodes.

$$\frac{\partial(\varepsilon\rho)}{\partial t}+\nabla\cdot(\varepsilon\rho\vec{u})=S_m \tag{10}$$

$$\frac{\partial(\varepsilon\rho\vec{u})}{\partial t}+\nabla\cdot(\varepsilon\rho\vec{u}\vec{u})=-\varepsilon p+\nabla\cdot\left[\varepsilon\mu\left(\nabla\vec{u}+(\nabla\vec{u})^T\right)\right]+S_u \tag{11}$$

where ε is the porosity, ρ (kg m^{-3}) is gas density, $\vec{u}$ (m/s) is the velocity vector, p (Pa) is the local gas pressure, μ (kg m^{-1} s^{-1}) is the dynamic viscosity, S_m (kg m^{-3} s^{-1}) and S_u (mol/m^{-3}(−|-) s^{-1}) are the source terms in the mass and momentum equations, which are listed in Table 2.

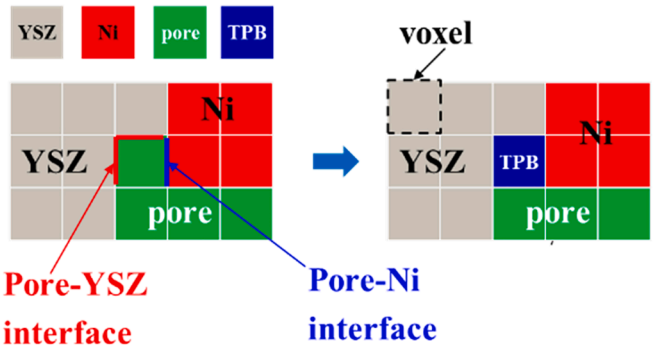

Fig. 4. Schematic of the determining TPB sites.

Table 4
Experimental conditions for the cell-scale model [22].

Parameters	Value
Pressure (Pa)	101,325
Temperature (K)	1023, 1073, 1123
H_2 molar fraction (inlet)	0.97/0.90/0.80
H_2O molar fraction (inlet)	0.03/0.10/0.20

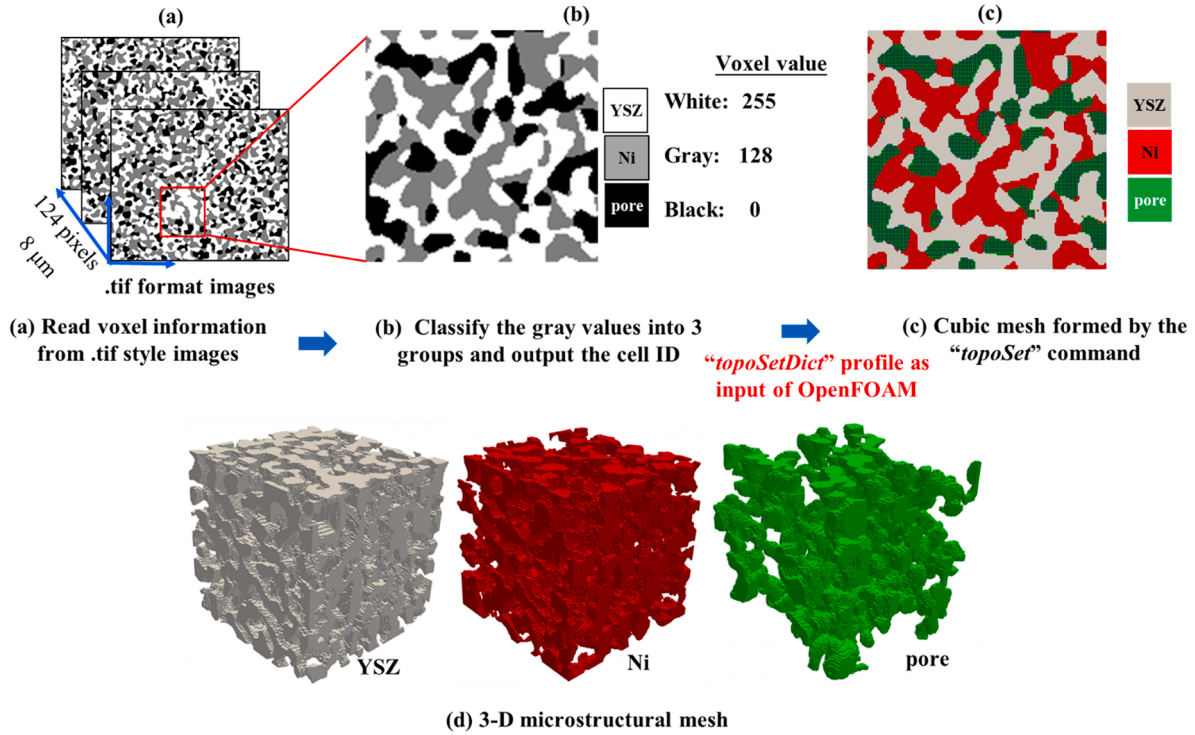

Fig. 3. Schematic diagram of the microstructural mesh generation in OpenFOAM, (a) original segmentated anode images, (b) transforming the cell indexes into OpenFOAM readable profile (topoSetDict), (c) the computational meshes used in OpenFOAM, and (d) 3D microstructural meshes of three different phases.

Table 5
Boundary conditions for the pore-scale model.

Distance from the electrolyte: l (anode-channel interface)	Distance from the electrolyte: 0 (anode-electrolyte interface)	Other boundaries
$X_i = X_{bulk}$	$\nabla X_i \cdot \vec{n} = 0$	symmetric
$\varphi_{ele} = \eta_{tot}$	$\varphi_{ion} = 0$	
$\nabla \varphi_{ion} \cdot \vec{n} = 0$	$\nabla \varphi_{ele} \cdot \vec{n} = 0$	

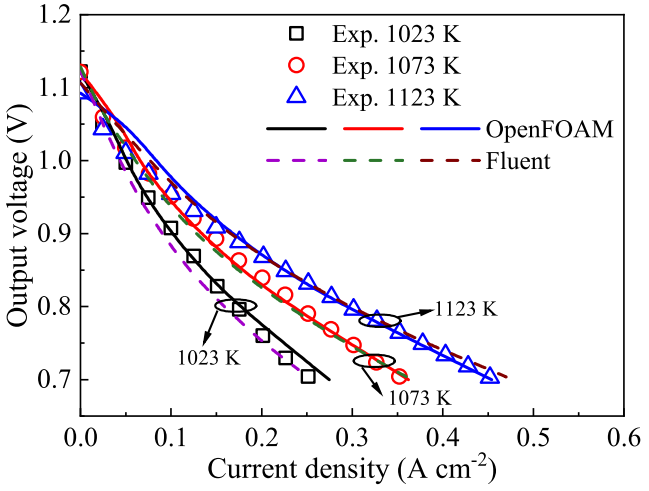

Fig. 5. Validation of the predicted polarization curves of the cell-scale model in OpenFOAM against the experiments [35] and the Fluent model [22].

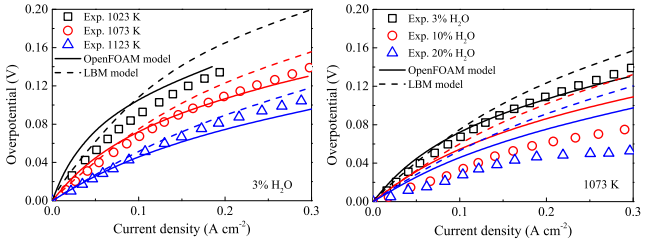

(a) Different temperatures (b) Different steam concentrations

Fig. 6. Comparison among the pore-scale models developed in OpenFOAM and LBM and the experiments [41] with respect to the relationship between overpotential and current density.

Porosity equals to unity in the channels.

Species conversation

The species transport inside SOFCs is solved in the ASL, anode, CSL, cathode, and gas channels.

$$\frac{\partial(\varepsilon\rho Y_i)}{\partial t} + \nabla\cdot\left(-\rho D_{\mathrm{eff},i}\nabla Y_i + \rho\vec{u}Y_i\right) = S_i \tag{12}$$

The cell-scale model considers both convective and diffusive transport in the gas channels and porous electrodes, as well as the molecular and Knudsen diffusion. $S_i$is the source term for species i.

The Knudsen diffusion coefficient ($D_{k,ij}$) is calculated by [22]:

$$D_{k,ij} = \frac{d}{3}\sqrt{\frac{8RT}{\pi M_{ij}}} \tag{13}$$

where d (m) represents the average pore diameter, R is universal gas constant (J/mol K^{-1}), T (K) is gas temperature. And the binary molecular diffusion coefficient $D_{i,j}$ is calculated by [22]:

$$D_{i,j} = \frac{0.0101T^{1.75}}{pM_{ij}^{1/2}\left[V_i^{1/3} + V_j^{1/3}\right]^2} \tag{14}$$

where V_i and V_j (m^{-3} mol^{-1}) are the special Fuller diffusion volumes, respectively. $M_{i,j}$ is defined as

$$M_{i,j} = \frac{2}{M_i^{-1} + M_j^{-1}} \tag{15}$$

where M_i and M_j are the molecular weight of specie i and j, respectively. And the effective diffusion coefficient $D_{\mathrm{eff},ij}$ is expressed as [22]:

$$\frac{1}{D_{\mathrm{eff},ij}} = \begin{cases} \dfrac{\sum_{j\neq i}\dfrac{x_j}{D_{ij}}}{1-x_i} \\ \dfrac{\tau}{\varepsilon}\left(\dfrac{\sum_{j\neq i}\dfrac{x_j}{D_{ij}}}{1-x_i} + \dfrac{1}{D_{k,ij}}\right) \end{cases} \tag{16}$$

where τ is the tortuosity and the value employed in the study is listed in Table 3.

Electrochemistry

The electrochemical reaction rates are calculated by the Butler-Volmer (BV) equations [22]:

$$J_{\mathrm{a}} = j_{0,\mathrm{a}}A_v\left(\exp\left(\alpha_{\mathrm{a}}\frac{2F\eta_{act}}{RT}\right) - \exp\left(-(1-\alpha_{\mathrm{a}})\frac{2F\eta_{act}}{RT}\right)\right) \tag{17}$$

$$J_{\mathrm{c}} = j_{0,\mathrm{c}}A_v\left(\exp\left(\alpha_{\mathrm{c}}\frac{4F\eta_{act}}{RT}\right) - \exp\left(-(1-\alpha_{\mathrm{c}})\frac{4F\eta_{act}}{RT}\right)\right) \tag{18}$$

where A_v (m2/m^{-3}(−|-)) is the reactive surface area per unit volume. α_{a} and α_{c} are the transfer coefficients. F is the Faraday's constant. $j_{0,\mathrm{a}}$ and $j_{0,\mathrm{c}}$ (A/m^{-2}(−|-)) represent the exchange current density of anode and cathode, which are determined by:

$$j_{0,\mathrm{a}}^{\mathrm{H_2}} = \gamma_{\mathrm{H_2}}\left(\frac{P_{\mathrm{H_2}}}{P_{ref}}\right)^m exp\left(-\frac{E_{act,\mathrm{a}}}{RT}\right) \tag{19}$$

$$j_{0,\mathrm{a}}^{\mathrm{CO}} = \gamma_{\mathrm{CO}}\left(\frac{P_{\mathrm{co}}}{P_{\mathrm{ref}}}\right)^n exp\left(-\frac{E_{act,\mathrm{a}}}{RT}\right) \tag{20}$$

$$j_{0,\mathrm{c}} = \gamma_{\mathrm{O_2}}\left(\frac{P_{\mathrm{O_2}}}{P_{\mathrm{ref}}}\right)^k exp\left(-\frac{E_{act,\mathrm{c}}}{RT}\right) \tag{21}$$

where m, n and k are reaction orders to fit the influence of operating pressure changes, and $\gamma_{\mathrm{H_2}}$, γ_{CO} and $\gamma_{\mathrm{O_2}}$ are the adjustable experiment fitting parameters. $E_{\mathrm{act,a}}$ and $E_{\mathrm{act,c}}$ (J/mol) are the activation energy in anode and cathode. See the values of these parameters in Table 3. In general, total overpotential η_{total} (V) consist of the ohmic overpotential activation overpotential η_{ohm} (V), the activation overpotential η_{act} (V) and concentration overpotential η_{con} (V). The total overpotential is calculated by the difference between output voltage and open circuit voltage. η_{act} is defined as $\eta_{\mathrm{act}} = \varphi_{\mathrm{ele}} - \varphi_{\mathrm{ion}}$ [18]. η_{ohm} (V) is calculated by Ohm's law as following:

$$\eta_{\mathrm{ohm}} = \frac{JL}{\sigma} \tag{22}$$

where L (m) is the thickness of the given conductive component and σ (S m^{-1}) the corresponding conductivity. The concentration overpotential η_{con} is calculated by deducting ohmic and activation overpotentials from the total overpotential.

Electronic potential φ_{ele} in the interconnects, SLs, anode and cathode is governed by the following equation:

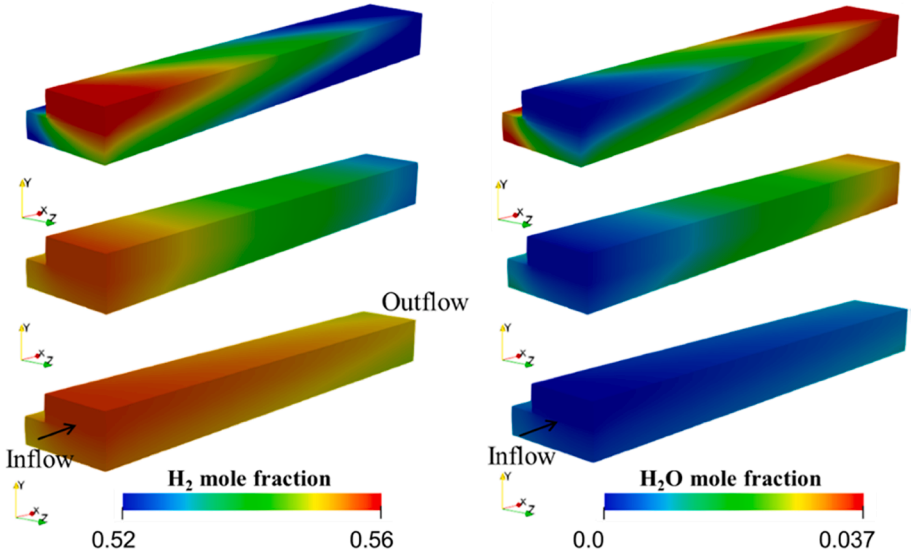

Fig. 7. Contours of H_2 and H_2O mole fraction at V_{out} = 0.7 V (top), 0.8 V (middle), and 1.1 V (bottom), operating temperature 1073 K.

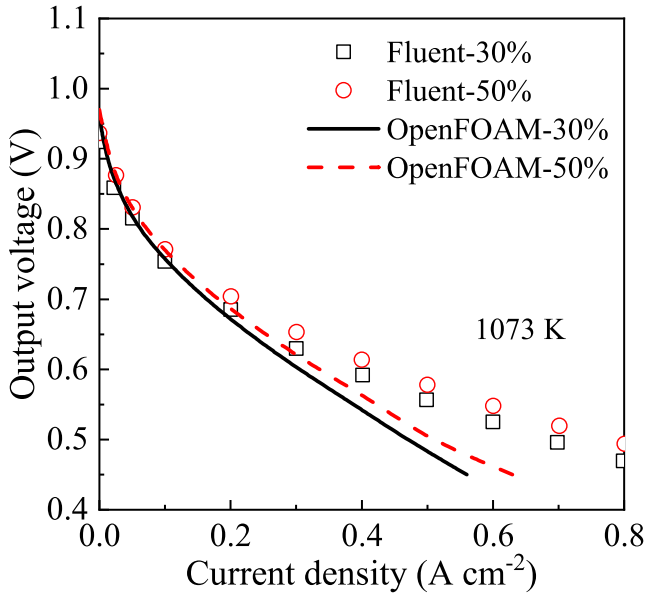

Fig. 8. Effects of different ratio of pre-reformed methane gas (30% and 50%) [42] and the comparison between the OpenFOAM and ANSYS Fluent models [22].

$$\tau_{con}\frac{\partial \varphi_{ele}}{\partial t} = \nabla\cdot\left(k_{ele}^{eff}\nabla\varphi_{ele}\right) + S_{ele} \tag{23}$$

Ionic potential φ_{ion} in anode and cathode and electrolyte is governed by the following equation:

$$\tau_{con}\frac{\partial \varphi_{ion}}{\partial t} = \nabla\cdot\left(k_{ion}^{eff}\nabla\varphi_{ion}\right) + S_{ion} \tag{24}$$

where τ_{con} is a time constant to relax the chemical kinetic reaction rates in the BV equations. The changes of the time term do not affect the final steady state of the cell model. The effective electron/ion conductivity in reaction layers are defined by:

$$k_{ele}^{eff} = \omega\left(\frac{1-\varepsilon}{\tau}\right)k_{ele} \tag{25}$$

$$k_{ion}^{eff} = (1-\omega)\left(\frac{1-\varepsilon}{\tau}\right)k_{ion} \tag{26}$$

where ω is the volume fraction of the electron conducting particles. And the electron/ion conductivity (k_{ele}/k_{ion}) is dependent on the temperature, and their definition can be found in Table 3. The temperature-dependent electron/ion conductivities are relevant to reveal the effect of different material properties on the cell performance and thus have been considered in both 2D [29] and 3D SOFC modelling [30].

The Nernst's equation is used to predict the open circuit voltage (E_{OCV}), which is calculated by:

$$E_{OCV,H_2} = -\frac{\Delta G}{n_e} + \frac{RT}{n_e F}ln\left[\frac{P_{H_2}^{l}\left(P_{O_2}^{l}\right)^{0.5}}{P_{H_2O}^{l}}\right] \tag{27}$$

$$E\frac{\Delta G}{n_e}\frac{RT}{n_e F}ln\left[\frac{P_{CO}^{l}\left(P_{O_2}^{l}\right)^{0.5}}{P_{CO_2}^{l}}\right]_{OCV,CO} \tag{28}$$

$$E_{OCV} = E_{OCV,H_2}\frac{\chi_{H_2}}{(\chi_{H_2}+\chi_{CO})} + E_{OCV,CO}\frac{\chi_{CO}}{(\chi_{H_2}+\chi_{CO})} \tag{29}$$

where ΔG (J/mol) represents the change of Gibbs free energy. n_e is the number of electrons. *PI* (Pa) stands for species partial pressure at the interface between electrode and electrolyte, and it is scaled based on the reference pressure (1 atm). Thus, the effect of concentration is taken into account in the Nernst equation as a concentration overpotential [31]. This means that the concentration overpotentials are represented by the variation of open circuit voltage caused by the concentration changes of reactants and products.

2.1.2. Boundary conditions

The co-flow pattern is assumed in all cases of this study, as shown in Fig. 2. A gas flow rate of 0.5 slpm hydrogen + 0.4 slpm nitrogen was introduced at the anode inlet, and 0.9 slpm air was used at the cathode inlet. The operating pressure is 1 atm, and three operating temperatures of 1023 K, 1073 K, and 1123 K were studied. The constant voltage mode is chosen in the present work by defining two different constant potential values at the two ends of cathode/anode interconnects based on the output voltage and E_{OCV}:

$$\varphi_{ele}^{a} = E_{OCV} - V_{out},\ \varphi_{ele}^{c} = 0 \tag{30}$$

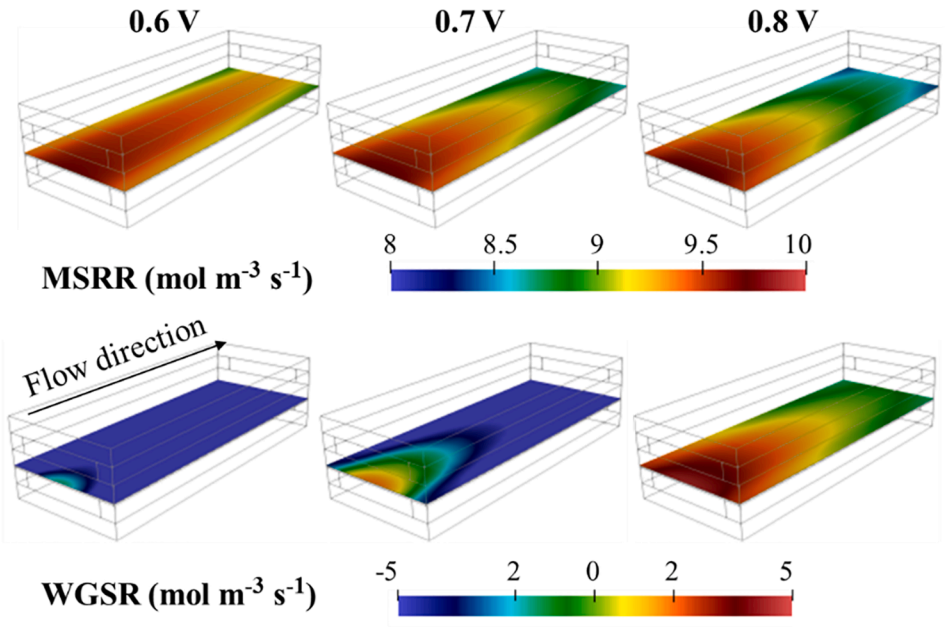

Fig. 9. Spatial distribution of the reaction rate in the case 30% pre-reformed gas with different output voltages. Top: MSRR, bottom: WGSR.

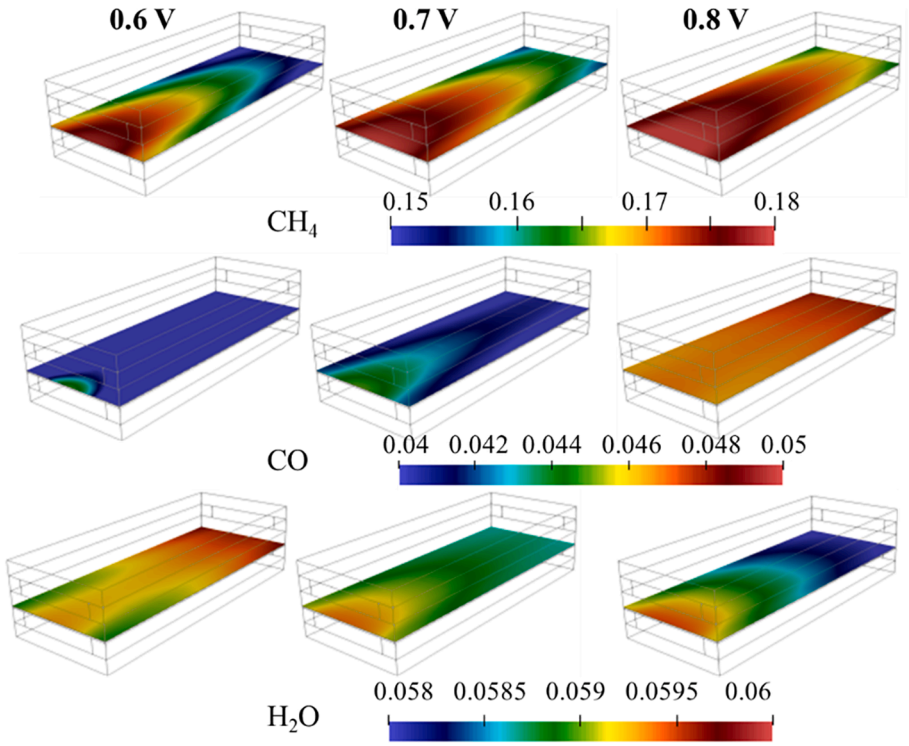

Fig. 10. Mass fraction of CH_4, CO, and H_2O at different output voltages in the case 30% pre-reformed methane.

2.1.3. Numerical procedure

The black solid lines shown in Fig. 2 indicate the boundaries for each region, while the dashed lines are the interior boundaries for the SL/electrode interfaces and channel/SL interfaces inside the anode part and cathode part. However, boundary conditions such as Dirichlet and Newman cannot directly be defined at these interior interfaces. Since the governing equations, for example electronic and ionic potentials are resolved in different regions, special treatments are necessary on the diffusion coefficient of an arbitrary passive scalar ϕ as

$$\frac{\partial \phi}{\partial t} = \nabla \cdot [\xi D \nabla \phi] \tag{31}$$

where D is the diffusion coefficient, and ξ is the zone indicator, which is defined as $\xi = 1$ in the selected regions, and $\xi = 0$ in other regions.

The geometry and cell mesh of the computational domain can be found in Table 1. The total number of mesh elements for a single cell is 240,000. Three coarse, intermediate and refined mesh along the channel direction, thickness direction and width direction were tested and the tested errors for the chosen mesh size in the study are below 1 %

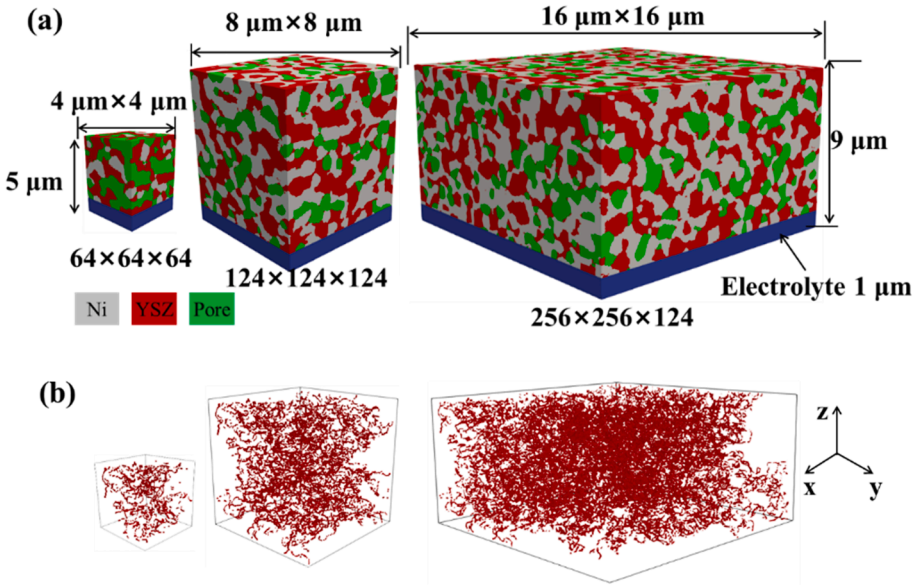

Fig. 11. The computational domains (a) and spatial active TPB distributions (b) for three different volumes.

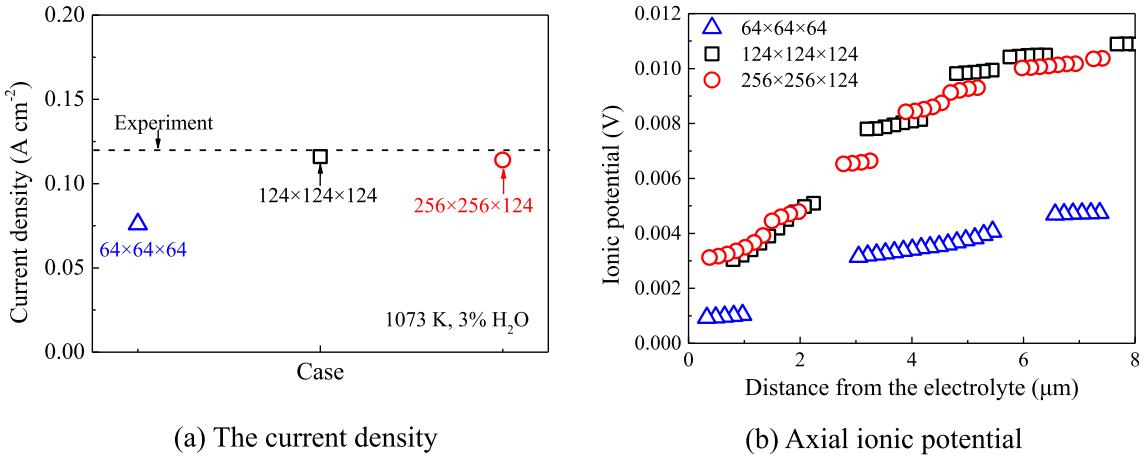

Fig. 12. The effects of volume element size on the current density and ionic potential distribution along the through-plane direction under operating conditions of V_{out} = 0.08 V, 1073 K and 3 % H_2O.

regarding operating current density and the averaged concentration. The cell-scale SOFC model is developed in the open source platform OpenFOAM. The pressure implicit with splitting of operators (PISO) algorithm is employed to solve the governing equations. The time term is discretized using a Euler scheme, and the convection, Laplacian, and gradient terms in the governing equations are discretized using a second-order scheme.

2.2. Pore-scale model

The pore-scale model focuses on the physical transports and electrochemical reactions in microstructural electrodes. Since the computational domain of the pore-scale model is small, the effect of fluid dynamics in the flow channel is ignored. In the current pore-scale model, the anode is only considered. The significant difference of the pore- and cell-scale models is the treatment of effective transport properties of the porous electrode. In pore-scale model, the effective transport properties, e.g. ionic and electronic properties are directly resolved based on the pore-scale microstructures instead of volume-averaged values. This requires sufficient resolution to resolve the electrode microstructures in a pore-scale model, which leads to a huge amount of computational mesh and limited size of computational domain. Therefore, the flow channel is excluded from the pore-scale model and the anode is only considered, which means only electrochemical and reactant diffusion are involved in the pore-scale model.

2.2.1. Governing equations

Charge transfer.

The governing equations of the pore-scale model are defined at the three phases and the TPB lines. The conduction of ions and electrons transport in the YSZ and Ni phases, respectively. And the charge conservation equations are shown in Eqns. (32) and (33), where J (Am^{-3}) is the electrochemical reaction rate. The time constant is consistent with the cell-scale model, see Table 3. The electronic/ionic conductivity can also be found in Table 3.

$$\tau_{con}\frac{\partial \varphi_{ele}}{\partial t} = \nabla\cdot(k_{ele}\nabla\varphi_{ele}) - J \tag{32}$$

$$\tau_{con}\frac{\partial \varphi_{ion}}{\partial t} = \nabla\cdot(k_{ion}\nabla\varphi_{ion}) + J \tag{33}$$

Electrochemistry.

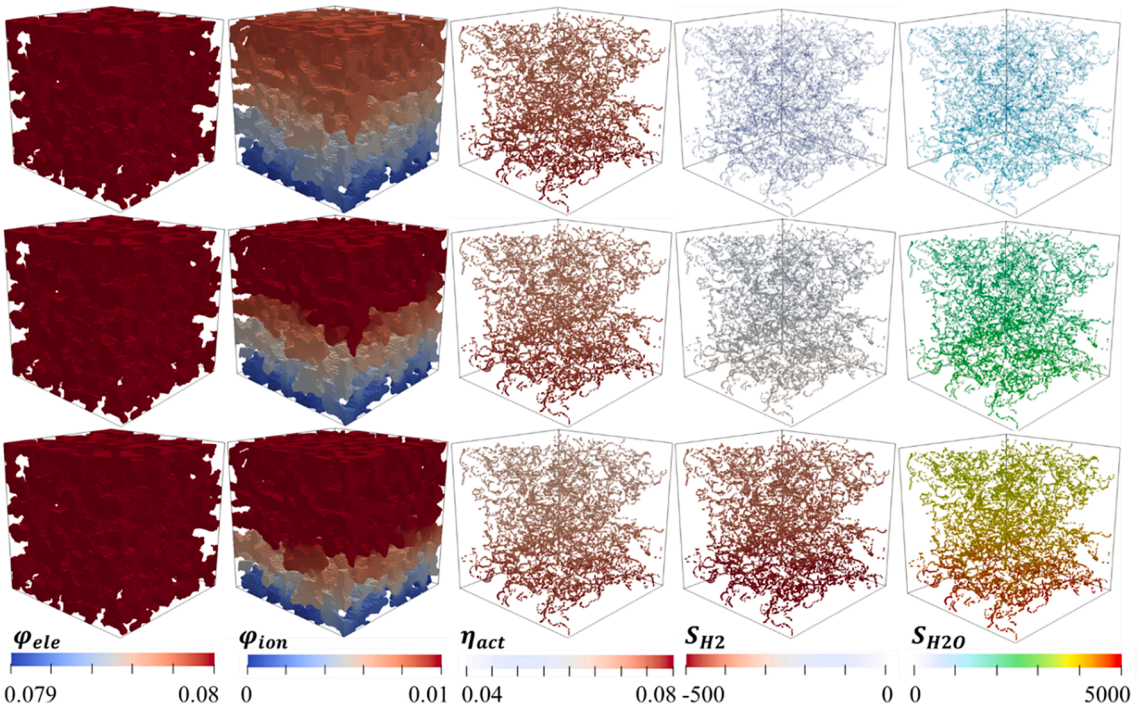

Fig. 13. Electronic and ionic potential distribution (φ_{ele} and φ_{ion}), activation overpotential (η_{act}, and source term for H_2 (S_{H2}), and H_2O (S_{H2O}) on the TPB sites. Top: 1023 K; middle: 1073 K; bottom:1123 K.

The electrochemical reaction occurs at the TPB lines is described by the BV equation below.

$$J = j_0\left(\exp\left(\frac{\alpha n F \eta_{act}}{RT}\right) - \exp\left(-\frac{\beta n F \eta_{act}}{RT}\right)\right) \tag{34}$$

α and β are the transfer coefficients. This BV equation was also employed by Li et al. [18] in a 3D pore-scale SOFC anode model. The exchange current density j_0 is fitted from the patterned anode experiments of Boer [32].

$$j_0 = 31.4 p_{H_2}^{-0.03} p_{H_2O}^{0.4} \exp\left(\frac{-1.52 \times 10^5}{RT}\right) \tag{35}$$

Mass transfer.

The Knudsen and molecular diffusion were considered in the current pore-scale model. And the species equation is described as follows:

$$\frac{\partial(\rho Y_i)}{\partial t} + \nabla\cdot\left(-\rho D_{\mathrm{eff},i}\nabla Y_i\right) = \begin{cases} 0 & \text{pore} \\ S_i^{tpb} & \text{TPB line} \end{cases} \tag{36}$$

where the mass source term S_i^{tpb} related to the electrochemical reactions in anode/cathode is only active at the TPB lines. The value of S_i^{tpb} is calculated as follow:

$$S_{H_2}^{tpb} = -M_{H_2}\frac{J}{2F} \tag{37}$$

$$S_{H_2O}^{tpb} = M_{H_2O}\frac{J}{2F} \tag{38}$$

2.2.2. Microstructural computational domain

The microstructures employed in the pore-scale model is extracted from a digital anode which was reconstructed by Xe PFIB-SEM technique with a resolution 65 nm [20]. The original size of the anode is large enough ($124 \times 110 \times 8\ \mu m^3$) to provide diverse small samples. The three phases in this segmented anode can be identified according to the voxel value, namely, YSZ (255), Ni (128), and pore (0). A technical challenge here is to transform these pixel-based images into computational meshes that can be recognised by OpenFOAM. To tackle it, all phase information was transformed into the readable profile (topoSetDict) of the OpenFOAM through MATLAB, as shown in Fig. 3. A series of mesh utilities (topoSet, splitMeshRegion) in OpenFOAM were employed to split a background mesh into three phases. Fig. 3 (b) and (c) compares the microstructure between the experimental segmentation images and the computational mesh generated by OpenFOAM. Fig. 3 (d) depicts the 3D domains of the phase YSZ, Ni, and pore, corresponding to the white, grey, and black region in the real image. The fractions of volume of three phases are 0.45, 0.34, and 0.21, respectively [33].

The ionic and electronic potential are resolved in the phase YSZ and Ni, respectively. As the electrochemical reaction occur at TPB sites, reasonably determining the TPB location is relevant to the model accuracy. Fig. 4 clearly shows how the TPB site is determined in the study. In this strategy, the cell in the pore region with a YSZ neighbour is marked. And only the same cell also having a Ni neighbour cell is regarded as the TPB site, where electrochemical reactions occur. It is implemented by finding the pore cell both having a pore-YSZ interface and a pore-Ni interface and this cell is marked as the TPB site. The electronic potential and ionic potential are solved in the Ni and YSZ region, respectively. The contiguous contact of the three phases (electronic, ionic, and gas phases) links the microstructure and the electrochemical performance of electrode.

2.2.3. Numerical procedure

The pore-scale model is also implemented in OpenFOAM. The numerical schemes and time step are same as the cell-scale model in Section 2.1.3. The parallel method Open-MPI coupled in OpenFOAM platform is employed for parallel simulation. Both the cell- and pore-cell scale models are developed based on the customised *chtMultiRegionFoam* solver in OpenFOAM 6.0. Each case took around 200,000 time steps to reach the steady state, which requires about 5 CPU hours computation using 4 Intel Xeon @ 2.93. GHz processors in parallel. The operating parameters are consistent with Kishimoto et al. [34] and list in Table 4. It is noted that H_2 and H_2O fractions in Table 4 refer to the feed conditions under the cell operating temperature and pressure. The boundary conditions used in the pore-scale model are shown in Table 5,

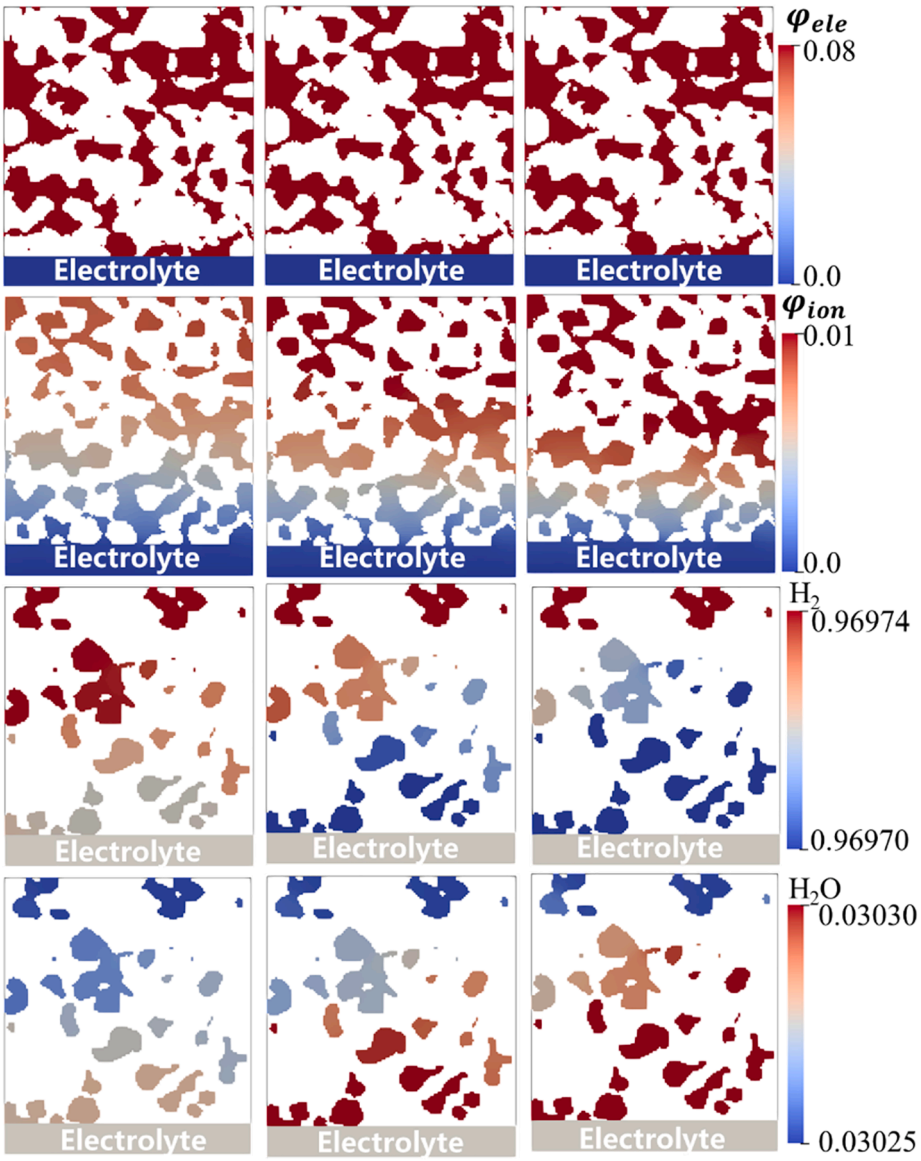

Fig. 14. Contours of electronic, ionic potential, H_2 and H_2O mole fraction under different temperatures. And the electrolyte is also included underneath the anode. Left: 1023 K, middle 1073 K, right 1123 K.

consistent with the previous study [18].

3. Results and discussion

In this section, the model validation is discussed at first. Both the cell- and pore-scale models are compared with experimental data and various numerical models that have been developed in other platforms. With the validated cell-scale model, the effects of using different fuel on the SOFC performance, i.e., pure hydrogen, 30 % and 50 % pre-reformed methane gas, are discussed in Section 3.2. The last section focuses on pore-scale physical and electrochemical characteristics revealed by the pore-scale model, including REV regarding operating current density and the comparison between synthetic microstructures and real microstructures reconstructed by Xe FIB-SEM.

3.1. Model validation

The validation of the cell-scale model is mainly focused on J-V_{out} curves. The structural parameters of the cell-scale model here are chosen according to the experiments of an anode-supported SOFC with a reaction area of 4 × 4 cm^2 [33]. All model parameters keep consistent with the Fluent model. The operating conditions of the model align with the three sets of experiments [35]. The chosen SOFC includes three different layers which are the key reaction sites, namely a 0.47–0.565 mm porous NiO/YSZ layer as anode, a 0.004–0.006 mm YSZ layer as the electrolyte and a 0.03–0.06 mm LSM/YSZ-LSM double layer as cathode. Although several studies have been conducted to validate SOFC models in OpenFOAM, large deviation and limited operating conditions are less compelling [36–38]. In this section, the performance of the SOFC is not only compared with experimental data under three different operating temperatures (1023 K, 1073 K and 1123 K) [35], but also with the multi-physics SOFC model developed in commercial CFD software ANSYS Fluent [22]. The comparison aims to demonstrate the reasonable prediction ability of the proposed cell-scale model. It is seen from Fig. 5 that the predicted polarization curves of cell-scale model in OpenFOAM agree well with those from the experiments and the Fluent model, which demonstrates that the accuracy of the current model is reasonable. The minor deviation between the OpenFOAM and Fluent models is possibly caused by the different numerical and discretization schemes employed in the two models. This has been verified by comparing various

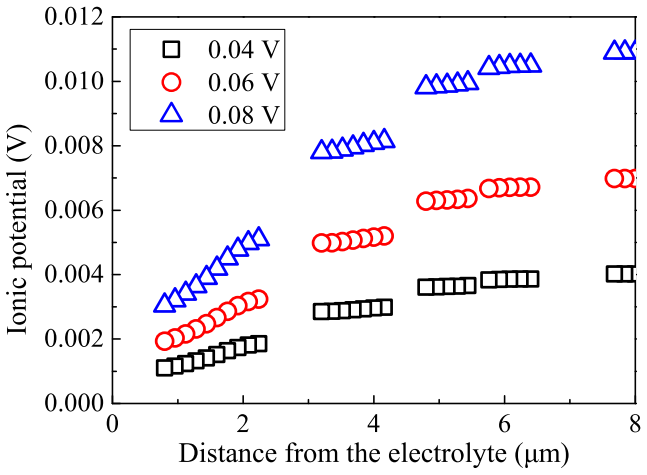

(a) The effect of total overpotential

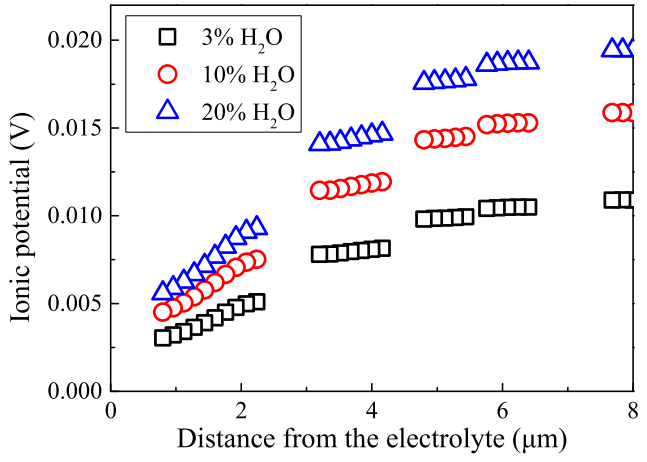

(b) The effect of steam concentration

Fig. 15. Ionic potential distributions along the through-plane direction under different total overpotentials and steam concentrations.

benchmark flow problems in OpenFOAM and Fluent, such as dispersed particle-laden flows [39] and bubbling fluidized bed hydrodynamics [40]. The computational costs of the two models are not compared in this study because of the absence of time information for the Fluent model [22]. For the OpenFOAM cell-scale model, a case normally takes 6 CPU hours to converge using 24 Intel Xeon @ 2.93. GHz processors in parallel.

The validation of the pore-scale model is mainly focused on *J-η* curves under different experimental operating temperatures and different vapor concentrations at the inlet. Since the experimental electrode microstructures were not available in both targeted experimental and numerical studies, a real SOFC electrode microstructure reconstructed by a Xe FIB-SEM is employed as the computational domain. A microstructural computational domain with a mesh number of 124 × 124 × 124 and mesh resolution of 65 nm is chosen for the validation. Fig. 6 compares the results of the pore-scale model in OpenFOAM with the experiments, as well as the results of a pore-scale SOFC model implemented via LBM [41]. It shows that the pore-scale model reasonably agrees with the experiments and the output voltage deviation is below 0.02 V under different temperatures. Compared with the LBM model, the OpenFOAM model underestimates the performance.

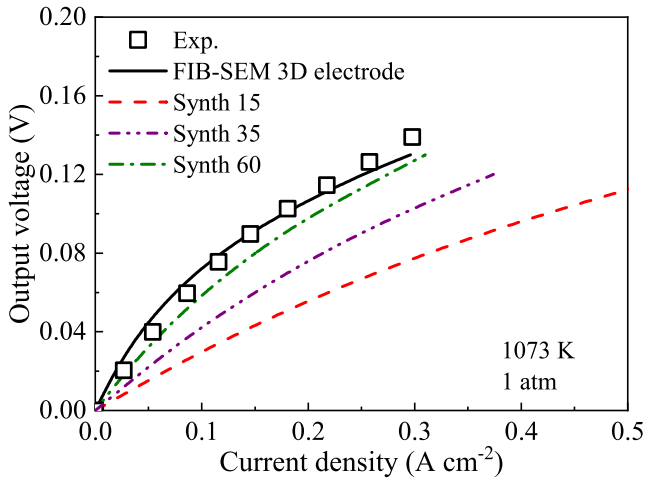

Fig. 16. The effects of different geometric standard deviations $\ln\sigma_g^{in}$ on the relationship between the total overpotential and current density. The experimental data is from Ref. [41]. The "FIB-SEM sample" solid line means the sample reconstructed by Xe FIB-SEM electrode microstructure.

This is possibly because of the different numerical schemes applied in the two models. The validation against experimental data and the results of the LBM model [41] is further conducted under three different steam concentrations, i.e. the steam including 3 %, 10 % and 20 % vapor, respectively, as shown in Fig. 6 b. It is seen that the current model overpredicts the overpotential in the case 10 % and 20 % H_2O. Similar deviation can also be seen in LBM pore-scale model, which even shows much larger deviation than the OpenFOAM model. There are two reasons that possibly cause the deviation. The first is that it is challenging to employ precisely same anode microstructures with the experiments, resulting in a slight difference in structural parameters. The second reason is related to assumptions in the pore-scale model. Similar with the study by Kanno et al. [41], the pressure in the pore-scale model is assumed as constant. Besides, the discrepancy between the pore-scale model and the experimental data is also attributed to the accuracy of the exchange current density model. As two relevant parameters in the exchange current density model, α and β heavily depends on the operating conditions, such as temperature and reactant concentration. Limited by the difficulties in measuring the exchange current density at various operating conditions, it is challenging to use semi-empirical models to accurately estimate exchange current density. Thus, the current model can only choose this limited exchange current density model for modelling. A similar discrepancy has been identified in the LBM model [41] and other data-driven exchange current density models [36].

3.2. *Effects of different fuels*

In this section, the cell-scale model is employed to investigate the effects of different fuel on the SOFC performance, i.e. pure hydrogen, 30 % and 50 % pre-reformed methane gas. The polarization curves of the case pure hydrogen under different temperatures have been shown in Fig. 5. The spatial distributions of reactant H_2 and product H_2O are shown in Fig. 7 under the operating temperature 1073 K and output voltage V_{out} = 0.7, 0.8 and 1.1 V. Low V_{out} means intense electrochemical reactions inside the SOFC, which leads to the quick consumption of H_2 and accumulation of H_2O downside the channel. Thus, high gradient of species along the channel is observed. It also shows that the H_2 concentration at the outlet is still high even with large electrochemical reaction rate (V_{out} = 0.7 V), which indicates that the remaining gas is still useful by redirecting into gas turbines to further increase the system efficiency.

The effects of different ratio of pre-reformed methane gases as fuel

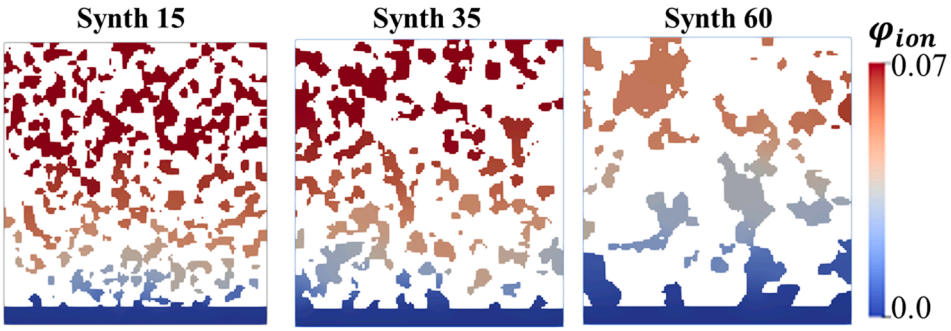

Fig. 17. The ionic potential distributions in different synthetic microstructures.

are also studied. The detailed fuel components are from Ref. [42], namely 30 % pre-reformed methane gas, including 17.1 % CH_4, 49.3 % H_2O, 2.94 % CO, 4.36 % CO_2, and 26.3 % H_2, and 50 % pre-reformed methane gas, including 11.5 % CH_4, 37 % H_2O, 2.7 % CO, 8.9 % CO_2, and 39.9 % H_2 in volume. It is seen in Fig. 8 that higher ratio of pre-reformed methane gas (50 %) contributes to higher output voltage. The results of the cell-scale model are also compared with a Fluent model [22]. Similar tendency between two models in predicting the effects of different pre-reformed methane gases are also seen from Fig. 8, which indicates that the accuracy of the developed cell-scale model in OpenFOAM. The discrepancy in the large current density range may be caused by two reasons. The first is the intrinsic difference between numerical schemes and discretization of OpenFOAM and Fluent. The other reason is the difference in thermal boundary conditions. In the Fluent model, a thermal adiabatic boundary condition was employed. While in the current model, the isothermal condition is considered.

The spatial distributions of reaction rate of the WGSR and MSRR, noted as R_{WGSR} and R_{MSRR} are shown in Fig. 9 to highlight the heterogeneity of the chemical reactions in the anode CL. High output voltages correspond to the low current density cases. As the reaction rates are calculated based on the partial pressure of reactants and products, the reaction rate can be negative, consistent with the previous work [23]. When the output voltage is low, for example, at $V_{out} = 0.6$ V, the intense electrochemical reactions consume H_2 rapidly, causing a large gradient of H_2 concentration. The reaction rate of the MSRR is higher at $V_{out} = 0.6$ V than the other two cases at the locations close to the outlet. The electrochemical reactions of H_2 are dominant and that of CO was not so intense and can be ignored according to the previous studies, e.g., modelling a SOFC with pre-reformed methane-based fuels [37], multi-physics modelling of planar SOFC stack [38] and pore-scale modelling of anode based on realistic electrode microstructures [41]. Portion of CO can be consumed by the WGSR, forming H_2, which further involves in the electrochemical reactions. The concentration of H_2O increases along the flow direction due to the vapor production at a low output voltage of $V_{out} = 0.6$ V, as shown in Fig. 10. The cell-scale model can be further employed as an efficient tool to evaluate the performance of SOFCs operating under various alternative fuels and further provide guidance for the design of flow channels and optimization of operating conditions to maximize the conversion efficiency.

3.3. Pore-scale physical and electrochemical characteristics

Electrode microstructures are always related to the heterogeneous electrochemical reactions, various transport phenomena and degradation in SOFCs. Therefore, a pore-scale model is favourable to understand physical and electrochemical behaviours at microporous level [43] and to quantify the relationship between structural characteristics and overall performance of SOFCs [44]. This section identifies the size of the representative element volume (REV) for the SOFC anode with the help of the multi-physics pore-scale SOFC model. In addition, the spatial distributions of a series of physical variables are also analysed under different operating conditions. To further study the effects of various electrode microstructures on SOFC performance, four different stochastically synthetic digital anode microstructures from Ref. [20] are also considered.

3.3.1. Representative element size with respect to current density

REV refers to the minimum volume on which a measurement can be made to represent the relevant characteristics of the whole. Normally, the REV should be about 10–30 times the average particle size [45], a region with 64^3 voxels is regarded as the REV size of a digital SOFC electrode according to the analysis of two-point correlation from Lombardo et al. [33]. In this section, three kinds of volume were chosen to confirm the REV size with respect to current density. The total mesh number for the small (64^3 voxels), intermediate (124^3 voxels), and large ($256^2 \times 124$ voxels) volumes is about 0.3, 2.1, and 8.8 million, respectively. The computational domains and TPB spatial distributions of three cases are shown in Fig. 11. Each voxel in three images is converted as one cell in the computational domain. The basic and large volumes both have an 8-μm height, which is the same as the experiments [20]. An electrolyte with a thickness of 1 μm is located below the microstructural anode, as shown in Fig. 11. The pore-scale model is employed to predict the current density of three volumes under $V_{out} = 0.08$ V. The effects of volume element size on the current density and the local distribution of the averaged ionic potential along the through-plane direction is shown in Fig. 12. It is seen from Fig. 12 (a) that small size (6^3) underpredicts the current density because it has lower active TPB densities than the other two volumes. As the volume size increases the prediction is nearly same, which means intermediate volume size 124^3 is the REV size for the anode in this study. Fig. 12 (b) also shows that the small volume significantly underpredicts the ionic potential along the through-plane direction. It is noted that the symbols in Fig. 12 (b) are discontinuous because ionic potential is only solved in the phase YSZ.

3.3.2. Spatial distribution of various physical variables

Fig. 13 shows the distributions of the electronic potential in the Ni phase and ionic potential in the YSZ phase at different operating temperatures. Since the electronic conductivity is much larger than the ionic conductivity, φ_{ele} is homogeneous due to the thin anode with a thickness of 8 μm. On the top of the anode, the ionic potential has larger values at higher operating temperatures, indicating high electrochemical reactions occur in the anode. And the absolute values for the H_2 and H_2O source term are larger close to the electrolyte, as shown in Fig. 13, indicating that intense electrochemical reactions take place in the vicinity of the electrode–electrolyte interface. Therefore, the activation overpotential is higher in the region, leading to inhomogeneous distribution of the activation overpotential and charge-transfer resistance [43]. It further demonstrates that homogeneous models are limited to consider microstructure-related physical behaviours.

The porosity, distributions of different phases, and even the volume fraction of each phase affect the electronic and ionic conductivity, and

the TPB densities [44]. The pore-scale model reveals the transfer of electron, ion, and gas in the microstructural anode. The contours of φ_{ele}, φ_{ion}, H_2 and H_2O mole fraction are shown in Fig. 14 which further highlights the different distribution of above physical variables in the anode under different temperatures. Since electrochemical reactions only occur on the TPB sites and the top of the anode adjacent to the fuel channel has the bulk of the fuel, the decrease of the H_2 mole fraction is very small. The diffusion of fuel from the channel can supplement the fuel consumption. The electrochemical reactions do not cause a high fuel concentration gradient because of the sufficient fuel supply [18]. The concentration overpotential is negligible. Since the electrochemical reactions mainly take place in the vicinity of the electrode–electrolyte interface with a thickness of 10–20 μm [43], more H_2O is accumulated closely to the electrolyte, as shown in Fig. 14. It also noted that electronic and ionic potentials, and the mass conservation equations are solved in different phases in the anode. Electrons can only transfer through the Ni phase, and ions can only conduct in the YSZ phase, and fuel and products can only be resolved in the pore. Thus, contours of φ_{ele}, φ_{ion} and species show different structures.

The effect of total overpotential (η_{tot}) and steam concentration on the ionic potential along the height direction is shown in Fig. 15. In the cases of high values of η_{tot} and high concentration of steam, the ionic potential increases at the location away from the electrolyte, which is consistent with the previous work [18]. Li et al. [19] compared the ionic potential from a homogeneous model and a heterogeneous model, finding that large variations are observed by considering the microstructure and the heterogeneous electrochemical reactions. Moreover, the ionic potential shows a quicker drop close to the electrolyte under higher total overpotential conditions, which is consistent with the results from the previous work, where higher gradient in ionic potential is observed in the YSZ phase. Generally, it is challenging to probe the presented spatial physical and electrochemical dynamics inside the electrode microstructures via experimental facilities. This challenge can be tackled by integrating the pore-scale model with advanced imaging techniques. The model fusion will provide deeper physical and electrochemical insights into high-performance electrode design and fabrication.

3.3.3. *Effect of electrode microstructures*

This section reports further studies of the effects of different structural parameters of the SOFC anode on the cell performance by using the pore-scale model. As a limited number of digital samples have been reconstructed by imaging experiments, three digital samples synthesized by a stochastic algorithm in the software DREAM.3D are employed here [20]. It is noted that the voxel size is 125 nm instead of 65 nm. These electrodes all include three phases and each phase has a specified log-normal feature size distribution. The geometric standard deviations, $\ln\sigma_g^{in}$, were 0.15, 0.35, and 0.6. The corresponding microstructures are expressed as synth 15, 35, and 60, respectively. Each microstructure has 124^3 voxels, which are taken from the synthetic microstructures images in Ref. [20]. Since the resolution for the synthetic electrodes is larger than the real one, the total height of the microstructure is 16.5 μm together with a 1-μm electrolyte. The electrochemical performance of the synthetic microstructures together with the real electrode from the experiments was compared in Fig. 16. By increasing the $\ln\sigma_g^{in}$, the number weighted particle size increases from 0.62 to 1.30 μm [20]. Larger particle size, for example, the synth 60 case decreases the TPB density [46], thus the reacting sites. Larger overpotential and lower current density are observed. It is seen from Fig. 17 that the synthetic electrodes have different microstructures and the synth 15 case has smaller sizes, which can provide more sites for the connecting three-phases. Therefore, the synth 15 microstructure shows the best electrochemical performance compared to the other synthetic microstructures.

4. Conclusions

In this study, two cell-scale and pore-scale solid models were developed in the open source platform OpenFOAM for solid oxide fuel cells (SOFCs). Two models were comprehensively validated against series of data, including experimental data, numerical results from multi-physics ANSYS Fluent model and lattice Boltzmann method (LBM). Reasonable agreement was observed among these datasets. The cell-scale model involves all relevant transport and electrochemical phenomena in SOFCs, which enables the accurate prediction of overall cell performance under different operating temperatures and fuels, as well as spatial distribution of reactants and products. The pore-scale model considers the porous microstructures of the anode, reactant diffusion and charges transfer to reveal the electrochemical dynamics at pore-scale level and highlight the importance of considering microstructures in the SOFC model to understand heterogeneous reactions in the electrode. The size of the representative element volume (REV) in the anode was identified with the help of pore-scale model. It is found that the size of 124^3 is needed to yield the representative current density of the whole. This size is larger than the size 64^3 which is derived by the structural indicator two-point correlation coefficient. The pore-scale model was further employed to study the effects of structural parameter, namely geometric standard deviations on the electrochemical performance of the anode. In conclusion, OpenFOAM is a potential multi-physics computational platform that is capable of accurately predicting both cell-scale and pore-scale performance and spatial information of SOFCs. The developed codes have been public to help the community to use them as research tools for various SOFC engineering problems.

CRediT authorship contribution statement

Wanhui Zhao: Conceptualization, Methodology, Software, Validation, Writing – original draft, Visualization, Funding acquisition. **Valerie J. Pinfield:** Writing – review & editing. **Huizhi Wang:** Writing – review & editing. **Jin Xuan:** Writing – review & editing. **Zhiqiang Niu:** Conceptualization, Methodology, Software, Validation, Formal analysis, Investigation, Visualization, Writing – original draft, Supervision, Project administration, Funding acquisition.

Declaration of Competing Interest

The authors declare that they have no known competing financial interests or personal relationships that could have appeared to influence the work reported in this paper.

Data availability

Data will be made available on request.

Acknowledgements

W. Zhao gratefully thanks the financial support from National Natural Science Foundation of China (Grant No. 52206187) and the Fundamental Research Funds for the Central Universities, Civil Aviation University of China (Grant No. 3122021044). Z. Niu would like to acknowledge the support of the Royal Society – K. C. Wong International Fellowship (NIF\R1\191864) from the Royal Society.

***Code** Availability*

The code of two SOFC solvers developed in OpenFOAM is available in the following code repository in the GitHub: https://github.com/JasonNiu288/Solid-Oxide-Fuel-Cell-Solvers-in-OpenFOAM.git. The repository includes the cell-scale and pore-scale SOFC solvers which allow researchers to modify and customise according to their specific

demands, as well as two showcase SOFC models employed in the study.

References

[1] Bao C, Wang Y, Feng D, Jiang Z, Zhang X. Macroscopic modeling of solid oxide fuel cell (SOFC) and model-based control of SOFC and gas turbine hybrid system. Prog Energy Combust Sci 2018;66:83–140.
[2] Wang K, Hissel D, Péra MC, Steiner N, Marra D, Sorrentino M, et al. A review on solid oxide fuel cell models. Int J Hydrogen Energy 2011;36:7212–28.
[3] Kupecki J, Motylinski K, Milewski J. Dynamic analysis of direct internal reforming in a SOFC stack with electrolyte-supported cells using a quasi-1D model. Appl Energy 2018;227:198–205.
[4] Shen S, Kuang Y, Zheng K, Gao Q. A 2D model for solid oxide fuel cell with a mixed ionic and electronic conducting electrolyte. Solid State Ion 2018;315:44–51.
[5] Zhu H, Kee R, Janardhanan V, Deutschmann O, Goodwin D. Modelling elementary heterogeneous chemistry and electrochemistry in solid oxide fuel cells. J Electrochem Soc 2005;152:A2427.
[6] Sohn S, Nam J, Jeon D, Kim C. A micro/macroscale model for intermediate temperature solid oxide fuel cells with prescribed fully-developed axial velocity profiles in gas channels. Int J Hydrogen Energy 2010;35:11890–907.
[7] Lin B, Shi Y, Ni M, Cai N. Numerical investigation on impacts on fuel velocity distribution nonuniformity among solid oxide fuel cell unit channels. Int J Hydrogen Energy 2015;40:3035–47.
[8] Zhan R, Wang Y, Ni M, Zhang G, Du Q, Jiao K. Three-dimensional simulation of solid oxide fuel cell with metal foam as cathode flow distributor. Int J Hydrogen Energy 2020;45:6897–911.
[9] Liu S, Kong W, Lin Z. Three-dimensional modelling of plannar solid oxide fuel cells and the rib design optimization. J Power Sources 2009;194(2):854–63.
[10] Kakac S, Pramuanjaroenkij ZX. A review of numerical modelling of solid oxide fuel cells. Int J Hydrogen Energy 2007;32:761–86.
[11] Bao C, Wang Y, Feng D, Jiang Z, Zhang X. Macroscopic modelling of solid oxide fuel cell (SOFC) and model-based control of SOFC and gas turbine hybrid system. Prog Energy Combust Sci 2018;66:83–140.
[12] Niu Z, Pinfield VJ, Wu B, Wang H, Jiao K, Leung DYC, et al. Towards the digitalisation of porous energy materials: evolution of digital approaches for microstructural design. Energ Environ Sci 2021;14:2549–76.
[13] Chen D, Wang H, Zhang S, Tade M, Shao Z, Chen H. Multiscale model for solid oxide fuel cell with electrode containing mixed conducting material. AIChE J 2015; 61:3786–803.
[14] Mozdzierz M, Berent K, Kimijima S, Szmyd J, Brus G. A multiscale approach to the numerical simulation of the solid oxide fuel cell. Catalysts 2019;9(3):253.
[15] Cai Q, Adjiman CS, Brandon NP. Modelling the 3D microstructure and performance of solid oxide fuel cell electrodes: computational parameters. Electrochim Acta 2011;56:5804–14.
[16] Wu C, Wang Y, Hou Y, Li X, Peng Z, Du Q, et al. Reconstruction and optimization of LSCF cathode microstructure based on Kinetic Monte Carlo method and Lattice Boltzmann method. Chem Eng J 2022;436:132144.
[17] Wang Y, Wu C, Zu B, Han M, Du Q, Ni M, et al. Ni migration of Ni-YSZ electrode in solid oxide electrolysis cell: an integrated model study. J Power Sources 2021;516: 230660.
[18] Li Q, Chai D, Zhang X, Li G. Three-dimensional microscopic modeling and activation thickness analysis of the anode of solid oxide fuel cells. Energy Fuels 2021;35:12495–506.
[19] Li Q, Chai D, Wang L, Zhang X, Li G. Fine three-dimensional simulation of the heterogeneous anode of a solid oxide fuel cell with direct internal reforming. Chem Eng Sci 2021;242:116747.
[20] Hsu T, Epting WK, Mahbub R, Nuhfer NT, Bhattacharya S, Lei Y, et al. Mesoscale characterization of local property distributions in heterogeneous electrodes. J Power Sources 2018;386:1–9.
[21] Beale SB, Choi H-W, Pharoah JG, Roth HK, Jasak H, Jeon DH. Open-source computational model of a solid oxide fuel cell. Comput Phys Commun 2016;200: 15–26.
[22] Wang Y, Zhan R, Qin Y, Zhang G, Du Q, Jiao K. Three-dimensional modeling of pressure effect on operating characteristics and performance of solid oxide fuel cell. Int J Hydrogen Energy 2018;43:20059–76.
[23] Ni M. Modeling and parametric simulations of solid oxide fuel cells with methane carbon dioxide reforming. Energy Convers Manage 2013;70:116–29.
[24] Haberman BA, Young JB. Three-dimensional simulation of chemically reacting gas flows in the porous support structure of an integrated-planar solid oxide fuel cell. Int J Heat Mass Transfer 2004;47:3617–29.
[25] Lehnert W, Meusinger J, Thom F. Modelling of gas transport phenomena in SOFC anodes. J Power Sources 2000;87:57–63.
[26] Jin X, Ku A, Verma A, Ohara B, Huang K, Singh S. The performance of syngas-fueld SOFCs predicted by a reduced order model (ROM): temperature and fuel composition effects. J Electro Soc 2018;165(10):F786–98.
[27] Xu H, Zhang H, Sun Q, Yang G, Ni M. Modelling of direct carbon solid oxide fuel cells with H2O and CO2 as gasification agents. Int J Hydrogen Energy 2017;42(23): 15641–51.
[28] Adams T, Barton P. A dynamic two-dimensional heterogeneous model for water gas shift reactors. Int J Hydrogen Energy 2009;34(21):8877–91.
[29] Shi Y, Wang H, Cai N. Direct two-dimensional electrochemical impedance spectra simulation for solid oxide fuel cell. J Power Sources 2012;208:24–34.
[30] Andersson M, Yuan J, Sundén B. SOFC modeling considering hydrogen and carbon monoxide as electrochemical reactants. J Power Sources 2013;232:42–54.
[31] Ni M. The effect of electrolyte type on performance of solid oxide fuel cells running on hydrocarbon fuels. Int J Hydrogen Energy 2013;38:2846–58.
[32] Boer Bd. SOFC Anode : hydrogen oxidation at porous nickel and nickel/yttria-stabilised zirconia cermet electrodes. The Netherlands: University of Twente; 1998.
[33] Gayon-Lombardo A, Mosser L, Brandon NP, Cooper SJ. Pores for thought: generative adversarial networks for stochastic reconstruction of 3D multi-phase electrode microstructures with periodic boundaries. npj Comput Mater 2020;6:82.
[34] Kishimoto M, Iwai H, Saito M, Yoshida H. Quantitative evaluation of solid oxide fuel cell porous anode microstructure based on focused ion beam and scanning electron microscope technique and prediction of anode overpotentials. J Power Sources 2011;196:4555–63.
[35] Hsieh Y, Chan Y, Shy S. Effects of pressurization and temperature on power generating characteristics and impedances of anode-supported and electrolyte-supported planar solid oxide fuel cells. J Power Sources 2015;299:1–10.
[36] Gnatowski M, Buchaniec S, Brus G. The prediction of the polarization curves of a solid oxide fuel cell anode with an artificial neural network supported numerical simulation. Int J Hydrogen Energy 2021.
[37] Takino K, Tachikawa Y, Mori K, Lyth SM, Shiratori Y, Taniguchi S, et al. Simulation of SOFC performance using a modified exchange current density for pre-reformed methane-based fuels. Int J Hydrogen Energy 2020;45:6912–25.
[38] Russner N, Dierickx S, Weber A, Reimert R, Ivers-Tiffée E. Multiphysical modelling of planar solid oxide fuel cell stack layers. J Power Sources 2020;451:227552.
[39] Greifzu F, Kratzsch C, Forgber T, Linder F, Schwarze R. Assessment of particle-tracking models for dispersed particle-laden flows implemented in OpenFOAM and ANSYS FLUENT. Eng Applications of Comput Fluid Mech 2016;10(1):30–43.
[40] Venier C, Urrutia A, Capossio J, Baeyens J, Mazza G. Comparing ANSYS Fluent and OpenFOAM simulations of Geldart A, B and D bubbling fluidized bed hydrodynamics. Int J Numer Meth Heat Fluid Flow 2020;30(1):93–118.
[41] Kanno D, Shikazono N, Takagi N, Matsuzaki K, Kasagi N. Evaluation of SOFC anode polarization simulation using three-dimensional microstructures reconstructed by FIB tomography. Electrochim Acta 2011;56(11):4015–21.
[42] Andersson M, Nakajima H, Kitahara T, Shimizu A, Koshiyama T, Paradis H, et al. Comparison of humidified hydrogen and partly pre-reformed natural gas as fuel for solid oxide fuel cells applying computational fluid dynamics. Int J Heat and Mass Transfer 2014;77:1008–22.
[43] Kishimoto M, Onaka H, Iwai H, Saito M, Yoshida H. Physicochemical impedance modeling of solid oxide fuel cell anode as an alternative tool for equivalent circuit fitting. J Power Sources 2019;431:153–61.
[44] Brus G, Raczkowski PF, Kishimoto M, Iwai H, Szmyd JS. A microstructure-oriented mathematical model of a direct internal reforming solid oxide fuel cell. Energy Convers Manage 2020;213:112826.
[45] Liu X, Zhou S, Yan Z, Zhong Z, Shikazono N, Hara S. Correlation between microstructures and macroscopic properties of nickel/yttria-stabilized zirconia (Ni-YSZ) anodes: Meso-scale modeling and deep learning with convolutional neural networks. Energy and AI 2022;7:100122.
[46] Timurkutluk B, Altan T, Toros S, Genc O, Celik S. Engineering solid oxide fuel cell electrode microstructure by a micro-modeling tool based on estimation of TPB length. Int J Hydrogen Energy; 46 24 13298-13317.